

Revision2

Specific roles of sodium for the formation process of manganese-
substituted octacalcium phosphate

YUKI SUGIURA^{1*}, MASANORI HORIE¹, AKIRA TSUCHIYA² and, YOJI MAKITA¹

¹*Health and Medical Research Institute, National Institute of Advanced Industrial Science and Technology (AIST), 2217-14 Hayashi-cho, Takamatsu, Kagawa, Japan 761-8576.*

²*Department of Biomaterials, Faculty of Dental Science, Kyushu University, 3-1-1, Maidashi, Higashi-ku, Fukuoka, Japan 812-8582.*

*Corresponding author

Dr. Yuki Sugiura

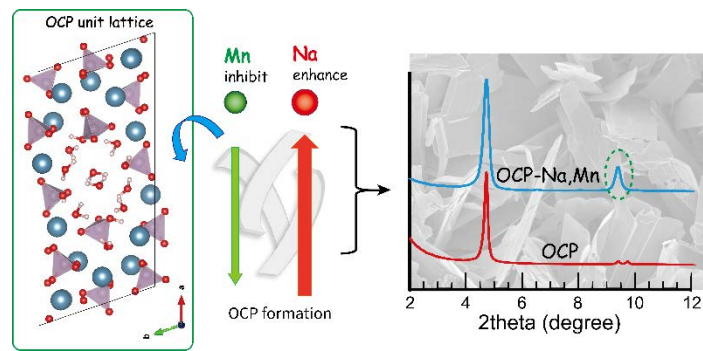
E-mail: yuki-sugiura@aist.go.jp

ABSTRACT

In the field of biomaterials, octacalcium phosphate (OCP) and biocompatible elements doped with OCP-based materials are attractive materials for new bone substitution because they could be used to control the bone remodeling process in patients with bone diseases. Manganese (Mn) might be a good substitutional element candidate because of its regulation process of bone remodeling for controlling osteo-cellular activities. However, Mn strongly inhibits the OCP formation. This study demonstrates that the sodium (Na)-induced OCP formation enhancing the $\text{HPO}_4\text{-OH}$ layer structure of the OCP can overcome this Mn inhibition effect. The Mn-substituted OCP can be fabricated from the co-existing solutions of Na and Mn. The results show that the Mn-substituted OCP-induced Na (OCP-Mn,Na) showed a 4.7° peak in the X-ray diffraction pattern. The sub-peaks at 9.2° and 9.7° of the OCP disappeared, but an extra peak at 9.3° was observed. The thermal stability of the OCP-Mn,Na was significantly lower than that of the conventional OCP because the layer structure of the OCP-Mn,Na was decomposed above $\sim 70^\circ\text{C}$. This ionic conjugation to Mn is a unique phenomenon for Na, unlike other cations.

KEYWORDS: Mn, octacalcium phosphate, ion substitution, Na, ion conjugation

TOC



INTRODUCTION

Octacalcium phosphate [OCP: $\text{Ca}_8(\text{PO}_4)_4(\text{HPO}_4)_2 \cdot 5\text{H}_2\text{O}$] is not only a main component of an immature bone, but is also an attractive material for the centerpiece of new biomaterials because of its excellent biocompatibility and components of Ca and PO_4 , which universally exist in biological beings (Brown et al. 1962; Davies et al. 2014; Dorozhkin and Epple 2002; Habraken et al. 2016). Its excellent bone-replacing ability is valuable for new bone substitutes (Kamakura et al. 2002; Sugiura et al. 2018; Suzuki 2010). Various studies have investigated the enhancement of its biocompatibilities by additives (Bracci et al. 2009; Gentleman et al. 2010; Mladenovic et al. 2014; Myrissa et al. 2016; Obata et al. 2009).

Biomaterial biocompatibilities are mainly dominated by their tissues and cellular responses. In the case of bone substitutes, osteo-cells, such as osteoblasts, osteoclasts, and osteocytes, play essential roles in the bone remodeling process. In addition, their viability, cytokine generation, and differentiation are closely controlled by biocompatible trace elements and molecules, such as Sr, Mg, Zn, and SiO_2 (Beattie and Avenell 1992; Boanini et al. 2012; Bracci et al. 2009; Mourino et al. 2012; Valanezhad et al. 2010). Accordingly, various studies have presented the control-releasing process of these biocompatible trace elements from biomaterials, such as calcium phosphate, alloys, and glasses, or

immobilized them onto the surface of biomaterials to control cell viability and differentiation (Myrissa et al. 2016; Obata et al. 2009; Saugo et al. 2018; Valanezhad et al. 2010; Wei et al. 2019; Sugiura et al. 2021). Both *in vitro* and *in vivo* studies have indicated that trace elements, such as Sr, Mg, and Zn-substituted calcium phosphates, might control and improve the bone remodeling process (Bracci et al. 2009; Forte et al. 2019; Matsunaga and Murata 2009; Mourino et al. 2012; Parra et al. 2017).

Manganese (Mn) is an important candidate because it influences the regulation of bone remodeling and increases the ligand-binding affinity of integrins, which mediate cellular interactions with extracellular matrix and activate cell adhesion (Luthen et al. 2007; Miola et al. 2014; Pabbruwe et al. 2004). Therefore, a Mn-doped OCP might be an attractive material for bone substitution. However, Mn inhibits the OCP formation, but induces formation of other calcium phosphate phases such as dicalcium phosphate hydrogen dihydrate [DCPD: $\text{CaHPO}_4 \cdot 2\text{H}_2\text{O}$], and amorphous calcium phosphate (ACP) (Boanini et al. 2010). So far, no studies have investigated how Mn-substituted calcium phosphate (including OCP) affects the bone remodeling process, especially its cellular effects (Armulik et al. 2000; Boanini et al. 2010; Medvecky et al. 2006). Thus, a fabrication process of Mn doping to OCP was needed for biological evaluation of whether Mn-doped OCP (and Mn-doped calcium phosphates) is a valuable candidate for a new

biomaterial or not.

We have been investigating how cations affect OCP formation. During the research, we discovered that the cationic conjugation process dominates a particular cation substitution into the OCP unit lattice (Sugiura and Makita 2018; Sugiura and Makita 2019; Sugiura et al. 2019). Na strongly induced OCP formation by enhancing the OCP layer structure considering the ionic radii similarity of Ca^{2+} (Sugiura and Makita 2018; Sugiura and Makita 2019; Sugiura et al. 2019). Therefore, we investigate herein whether or not the inducing property of Na could overcome the Mn inhibition for OCP to fabricate a Mn-substituted OCP.

EXPERIMENTAL METHOD

Evaluation of the Na effect for OCP formation with Mn

All reagents were purchased from FUJI Film Wako Pure Chemical Industries Inc. (Japan) as reagent-grade materials. H_3PO_4 was diluted using distilled water to 2.0 mol/L H_3PO_4 . NaCl and $\text{MnCl}_2 \cdot 4\text{H}_2\text{O}$ were dissolved into distilled water to prepare 20 mL of a series of cocktail solutions containing 100 mmol/L H_3PO_4 , 0–100 mmol/L MnCl_2 , and 0–5 mol/L NaCl. The initial pH of the solutions was ~ 0.5 .

CaCO_3 powder (0.50 g; 5 mmol) was immersed into 20 mL of the prepared

solutions containing various concentrations of 100 mmol/L H_3PO_4 with Na and Mn. The molar ratios of Mn/Ca and Na/Ca were 0.0 to 0.4 and 0.0 to 20.0, respectively. The mixtures were sealed after the initially formed CO_2 was released by mixing. They were then incubated at 60 °C for 1 day and 3 days. The treated samples were washed using distilled water and 99.5% ethanol for several times to remove the residual immersion solution and subsequently dried in an oven at 40 °C overnight. The final pH values of the reacting solutions were measured using a pH electrode (LAQUA ToupH 9615S-10D) connected to a pH meter (Horiba Co. D-72, Kyoto, Japan).

Evaluation of other metal ion effects for the OCP formation with 100 mmol/L Mn

The sample preparation method was similar to that in previous section. Instead of NaCl, 5 mol/L LiCl, KCl, RbCl, CsCl, MgCl_2 , and SrCl_2 was briefly dissolved into 100 mmol/L of MnCl_2 and H_3PO_4 solutions.

Characterization

The samples' crystallographic information was obtained by X-ray diffraction (XRD: MiniFlex600, Rigaku Co., Japan) at an acceleration voltage and current of 40 kV and 15 mA, respectively. The diffraction angle was continuously scanned over 2θ values

ranging from 3° to 70° at 5°/min for characterization and from 2° to 12° at 1°/min for crystallographic parameter analysis. The lattice parameters of the OCP crystals in the obtained XRD patterns of the samples were determined by Rietveld analysis using PDXL2 software (Rigaku Co., Japan). In this calculation, we used the structure model of the OCP crystal structure from Brown et al. (1962) as the initial model. In this case, peak at 9.38° was defined as OCP $d(110)$.

The vibrational spectra of the samples were characterized by Fourier transform infrared spectroscopy (FT-IR: Nicolet NEXUS670, Thermo Fisher Scientific, Co., USA) using a triglycine sulfate detector (32 scans, 2 cm⁻¹ resolution) with an attenuated total reflection prism made of GeSe. The atmosphere was the background for conducting the measurements.

The fine structure of the samples was assessed by field-emission scanning electron microscopy (FE-SEM: JSM-6700F, JEOL Co., Japan) at a 5 kV acceleration voltage. The samples were sputter-coated using Os to prevent surface charge accumulation.

The chemical states of the samples were characterized using an X-ray photoelectron spectrometer (XPS: K-Alpha, Thermo Fisher Scientific Co., USA) equipped with a monochromatic X-ray source (Al K α) operated at 12 kV and 6 mA; the pressure in the sample chamber was $\sim 1.4 \times 10^{-6}$ Pa. The spot size of the incident beam

was set to 400 μm . The binding energies were normalized to the C1s peak at 284.80 eV.

Before measurements, the samples were embedded into light-curing resin that consisted of 90% hydroxyethyl methacrylate (HEMA, FUJIFILM Wako Pure Chem Inc., Japan) and 10% diurethane dimethacrylate (UDMA, Sigma-Aldrich Co., USA) with camphorquinone and 4-(dimethylamino)benzoic acid ethyl ester (Sigma-Aldrich Co., USA) as initiator agents.

The Ca, P(PO_4), Na, and Mn contents of the samples were measured by inductively coupled plasma atomic emission spectroscopy (ICP–AES: 5110VDV, Agilent Technology Co., Japan) after they were dissolved in 2% HNO_3 solution.

The thermal behavior of the samples was determined by thermogravimetry–differential thermal analysis (TG–DTA; Thermo-Plus, TG8110, Rigaku Co., Japan) with 10 $^\circ\text{C}/\text{min}$ heating rate.

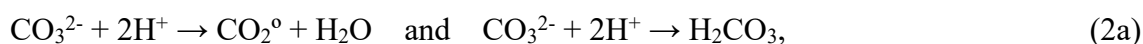
RESULT AND DISCUSSIONS

We employed a simple reaction process of CaCO_3 and H_3PO_4 (+ MnCl_2 and NaCl). The reacting solution pH is an important factor for the OCP formation because the calcium phosphate phases are controlled by the solution pH. When CaCO_3 is immersed into H_3PO_4 (+ MnCl_2 and NaCl meaning as acidic phosphate solutions) it dissolves. The

CaCO₃ dissolution reactions are complex, but for the purposes of this contribution they can be simplified to



in acidic solutions the CO₃²⁻ reacts with H⁺:



and in near-neutral pH solutions CO₃²⁻ and H⁺ produce bicarbonate:



For these reactions, pH of solutions increases with CaCO₃ dissolution because the CO₃²⁻ reacts with H⁺. As pH increases from the initial conditions, the solubility of the calcium phosphates decreases, thus, calcium phosphate crystalline phases such as OCP are likely to form (Vereecke and Lemaitre 1990). Although for calcium phosphate fabrication it was a hard to control the solution pH using this method, the advantages of this method for the

calcium phosphate fabrication was obtaining chemically pure calcium phosphate phases without any residual cations, which are normally employed to adjust the pH.

Figure 1 shows the pH values of the reacting solutions after 1 and 3 days. After 1 day, the pH values of the reacting solutions decreased with the increase of the Na and Mn concentrations. After addition of CaCO₃ the pH values of all the reacting solutions were weakly acidic to neutral, which was suitable for the OCP formation. After 3 days, the pH values of the reacting solutions slightly increased compared to those after 1 day. Therefore, the reactions were still proceeding at 3 days.

The treated materials were characterized by XRD. Figure 2 depicts the wide-scan XRD patterns of the treated materials at 1 day. In Mn-0 mmol/L, a monophasic OCP was formed below 2 mol/L Na, while hydroxyapatite [HAp: Ca₁₀(PO₄)₆(OH)₂] was the main component in 5 mol/L Na. Below the 20 mmol/L Mn concentration, the treated materials were mainly OCP. Above the 20 mmol/L Mn concentration with a low Na concentration, calcium hydrogen phosphate dihydrate [DCPD: CaHPO₄·2H₂O] and manganite [MnO(OH)] were mainly formed. On the contrary, for a high Na concentration, DCPD and manganite disappeared, but OCP was formed. CaCO₃ also significantly remained.

The fine peak analysis study indicated that the peaks of the OCP in both high Na and Mn concentrations were different (Figure 3). Although the OCP in 50 mmol/L Mn

with 5 mol/L Na and in 100 mmol/L Mn with 5 mol/L Na showed the strongest peak at 4.7°, which corresponded to OCP $d(100)$ without peaks at 9.2° (OCP $d(200)$) and 9.7° (OCP $d(110)$), it showed an extra peak at 9.3°.

OCP, probably Mn-doped OCP, may have been obtained in the systems with both high Na- and Mn-solutions. However, the samples contained not only OCP, but also CaCO₃ as a residual material, which must be removed to evaluate well the properties of OCP formed in the Mn-containing solutions. Accordingly, we performed two further evaluations to obtain a highly pure Mn-substituted OCP by longer reaction time or CaCO₃ amount reduction. As the first step, we simply increased the treating time from 1 day to 3 days. Figure 4 illustrates the wide-scan XRD patterns of the treated samples at 3 days. The ratio of OCP in each sample in all the Mn–Na systems is slightly attenuated, but that of HAp and manganite increased (Figure 5). In the case of 100 mmol/L with 5 mol/L Na, the intensities of OCP (Mn-substituted OCP) significantly decreased, whereas those of MnO(OH) significantly increased. This phenomenon suggests that the Mn-substituted OCP decomposed to MnO(OH) gradually. Thus, the reaction time elongation was a disadvantage for the OCP formation in Mn-containing systems. Note, however, that the analysis results are valuable for further investigation. We summarized the synthesized phases in the Na–Mn system in Figure 6.

We evaluated the lattice parameters of OCP in the systems with Na and Mn. Some of conditions were absent because we could not obtain reliable peaks of OCP. Figure 7 shows the lattice parameters of the OCP samples. In the case of the a-axis, we hardly observed the relationships between Mn concentrations and lattice parameters of OCP samples. However, as Na concentration increased, lattice parameters of samples formed of low Mn concentration (<20 mmol/L) were decreased whereas they increased in samples formed of high Mn concentration (<50 mmol/L). In the case of the b-axis, except for the Mn-100 mmol/L experiments, no significant alteration of lattice parameters was observed. In the case of the c-axis, as Mn concentration increased, lattice parameters of the samples decreased whereas as Na concentration increased, they were slightly increased.

We then reduced the amount of CaCO₃ starting materials. Figure 8 illustrates the XRD patterns of the synthesized products with various amounts of added CaCO₃ in the Na-5 mol/L and Mn-100 mmol/L systems. No CaCO₃ peaks were observed when the CaCO₃ amount was reduced to 0.25 g, which is half the value in the initial investigation. We then investigated the chemical composition of OCP (OCP-Mn,Na) by ICP-AES measurements. The Ca, Na, Mn, and P(PO₄) contents of OCP-Mn,Na were 23.7 ± 1.7, 18.3 ± 2.6, 12.7 ± 1.6, and 45.2 ± 0.7 at%, respectively.

To confirm the chemical state of Mn, we performed XPS measurement of samples. XPS was the only method to confirm chemical state of ferromagnetic element containing materials. Figure 9 showed XPS spectra of OCP-Mn,Na and OCP-Na (conventional OCP) for facilitate comparison. The peak top of Mn $2p$ was 641.25 eV, which value was close to that of MnO and MnSO₄ as Mn²⁺ composite (Zhong et al. 2017). Further, the chemical composition of OCP-Mn,Na is given as $\sim\text{Ca}_{3.14}\text{Na}_{1.68}\text{Mn}^{2+}_{2.43}\text{H}_{4.69}(\text{PO}_4)_6 \cdot n\text{H}_2\text{O}$ when the Mn ions were formed as Mn²⁺. It was suggested that the chemical composition of OCP-Mn,Na contained numerous H⁺ and water molecules.

The FT-IR analysis indicated the Mn substitution modes of OCP in OCP-Mn,Na. The XRD analysis already indicated that Mn substitution affected the OCP unit lattice. The vibration modes of the six PO₄ molecules labeled as *P1* to *P6* PO₄ (Berry and Baddiel 1967; Sugiura and Makita 2018), which comprised OCP, could be determined by taking advantage of the low symmetrical OCP crystal structure (*P-1*) for the spectroscopic method. In this measurement, conventional OCP (fabricated without Na and Mn) and OCP(Na) (fabricated with 2 mol/L Na) were used as references. Figure 10 shows the FT-IR spectra of OCP-Mn,Na, conventional OCP, and Na-doped OCP (OCP(Na)) for comparison. In OCP-Mn,Na, the band corresponded to *P3* PO₄ located in the HAp layer, and the strongest OCP band disappeared. Accordingly, *P5* PO₄ bands that corresponded

to the $\text{HPO}_4\text{-OH}$ layer structure significantly shifted. In other words, Mn (with Na) affected the typical OCP crystal structure.

The thermal behavior of the samples (i.e., thermal stability) could be evaluated through the TG-DTA method. Similar to the FT-IR samples, the curves of the conventional OCP and the Na-substituted OCP (OCP(Na)) were mentioned for comparison. Figure 11 presents the TG-DTA curves of OCP-Mn,Na. During the heating process, two DTA peaks were observed for the conventional OCP, that is, the evaporation of the adsorbing moisture ($\sim 70^\circ\text{C}$) and the decomposition of the $\text{HPO}_4\text{-OH}$ layer structure ($\sim 150^\circ\text{C}$). Meanwhile, OCP-Mn,Na showed a decomposed $\text{HPO}_4\text{-OH}$ layer structure below 70°C . In conclusion, the thermal stability of OCP-Mn,Na was much lower than that of the conventional OCP.

The fine structure of OCP-Mn,Na was determined by SEM. Figure 12 presents the SEM micrographs of the samples. All samples showed plate-like crystals ranging from several μm in size with a typical OCP morphology. For the Mn-containing samples, the aspect ratio of the plate-like crystals slightly decreased; however, a significantly morphological alternation was hardly observed.

As a further mechanical study on how conjugated cations assist Mn substitution, we will investigate how other cations affect the Mn substitution into the OCP unit lattice

by cation conjugation. To confirm this, we changed the additive cations Na to other metals. Figure 13 illustrates the XRD patterns of the treated samples. For alkali metal, Mg, and Sr, no evidence was found as regards the conjugation processes inducing the OCP formation.

Mn substitution into the OCP unit lattice by Na conjugation is a unique phenomenon. The similarity of the ionic radii of Na⁺ (1.02 Å) and Ca²⁺ (1.00 Å) caused Na solid-solutional substitution into the OCP unit lattice. This process enhanced the OCP layer structure, especially the HPO₄-OH layer structure, because Na substituted the conjugated site of *P5* PO₄, which was the root of the HPO₄-OH layer structure. However, the ionic radii of the cations can hardly describe this phenomenon because the ionic radii of Mn²⁺ was 0.80 Å. Therefore, large ionic radii cations, such as K, NH₄, Sr, and Rb, are more likely to perform substitution in the conjugation process.

The FT-IR spectra indicated that the Mn-substituted site was not the *P5* PO₄ conjugated site, but the *P3* PO₄ conjugated site located in the HAp layer structure of OCP. Several previous investigations derived the hint that Mn induced DCPD, even though a relatively high pH condition is preferential for the HAp (and OCP) formation. (Boanini et al. 2010; Matsunaga and Murata 2009) The FT-IR observation suggested that Mn inhibited the HAp-like structure formation, while Na particularly induced the HPO₄-OH

layer structure of OCP. This phenomenon also induced the side parts of the $\text{HPO}_4\text{-OH}$ and HAp layer structures. The OCP formation was then induced by Na yielding the Mn inhibiting effect (see TOC).

DCPD and OCP-Mn,Na decomposed to form OCP and manganite as time passes. Manganite is a Mn-rich material. Therefore, the remaining Ca and PO_4 from DCPD and OCP-Mn,Na re-reacted to form OCP because Mn was removed from the reaction systems as manganite. The thermal analysis with the OCP-Mn,Na material evolution indicated that OCP-Mn,Na had a metastable phase with very restricted kinetical and thermodynamical regions that may be regarded as no longer the OCP group.

IMPLICATIONS

This study investigated the effect of Na to Mn substitution to OCP. In cases of high Na concentration, Mn could be substituted into the OCP unit lattice as the $P3 \text{ PO}_4$ conjugated site. This process was not an ionic radii difference conjugation process, but originated from a typical phenomenon by specific Na inducing the $\text{HPO}_4\text{-OH}$ layer structure. The thermal stability of the fabricated OCP-Mn,Na was much lower than that of the conventional OCP. In the future work, we will evaluate the OCP-Mn,Na cellular responses to feasibility for bone substitution.

ACKNOWLEDGEMENTS AND FUNDING

This study is financially supported by the priority issue of the Health Research Institute, National Institute of Advanced Industrial Science and Technology (AIST), research grant, the foundation for the promotion of ion engineering and, KAKENHI for Young Researcher, JP19K19081. We thank Drs. Y. Uryu and T. Nakanishi for helping with FT-IR measurements. This study is partially supported by the Research Center for Industrial Science & Technology, Kagawa Industry Support Foundation (RIST Kagawa).

REFERENCES CITED

Armulik, A., Svineng, G., Wennerberg, K., Fassler, R. and, Johansson, S. (2000) Expression of Integrin Subunit β 1B in Integrin β 1-Deficient GD25 Cells Does Not Interfere with α V β 3 Functions. *Experimental Cell Research*, 254, 55-63.

Beattie, J.H. and, Avenell, A. (1992) Trace element nutrition and bone metabolism. *Nutrition Research Reviews*, 5, 167-188.

Berry, E.E. and, Baddiel, C.B. (1967) Some assignments in the infra-red spectrum of octacalcium phosphate. *Spectrochimica Acta*, 23A, 1781-1792.

Boanini, E., Gazzano, M., Rubini, K. and, Bigi, A. (2010) Collapsed Octacalcium Phosphate Stabilized by Ionic Substitutions. *Crystal Growth & Design*, 10 (2010) 3612-3617.

Boanini, E., Torricelli, P., Fini, M., Sima, F., Serban, N., Mihailescu, I.N. and, Bigi, A. (2012) Magnesium and strontium doped octacalcium phosphate thin films by matrix assisted pulsed laser evaporation. *Journal of Inorganic Biochemistry*, 107, 65-72.

Bracci, B., Torricelli, P., Panzavolta, S., Boanini, E., Giardino, R. and, Bigi, A. (2009) Effect of Mg^{2+} , Sr^{2+} , and Mn^{2+} on the chemico-physical and in vitro biological properties of calcium phosphate biomimetic coatings. *Journal of Inorganic Biochemistry*, 103, 1666-1674.

Brown, W.E., Smith, J.P., Lehr, J.R. and, Frazier, A.W. (1962) Crystallographic and Chemical Relations between Octacalcium Phosphate and Hydroxyapatite. *Nature*, 196, 1050-1055.

Davies, E., Muller, K.H., Wong, W.C., Pickard, C.J., Reid, D.G., Skepper, J.N. and, Duer, M.J. (2014) Citrate bridges between mineral platelets in bone, *Proceeding of the National Academy of Science of USA*, E1354-E1363.

Dorozhkin, S.V. and, Epple, M. (2002) Biological and medical significance of calcium phosphates. *Angewandte Chemie International Edition*, 41, 3130–3146.

Forte, L., Sarda, S., Torricelli, P., Combes, C., Brouillet, F., Marsan, O., Salamanna, F., Fini, M., Boanini, E. and, Bigi, A. (2019) Multifunctionalization Modulates Hydroxyapatite Surface Interaction with Bisphosphonate: Antiosteoporotic and Antioxidative Stress Materials. *ACS Biomaterial Science and Engineering*, 5, 3429-3439.

Gentleman, E., Fredholm, Y.C., Jel, G., Lotfibakhshaiesh, N., O'Donnell, M.D., Hill, R.G., Stevens, M.M. (2010) The effects of strontium-substituted bioactive glasses on osteoblasts and osteoclasts in vitro. *Biomaterials*, 31, 3949–3956.

Habraken, H., Habibovic, P., Epple, M. and, Bohner, M. (2016) Calcium phosphates in biomedical applications: materials for the future? *Material Today*, 19, 69-87.

Kamakura, S., Sasano, Y., Shimizu, T., Hatori, K., Suzuki, O., Kagayama, M. and, Motegi, K. (2002) Implanted octacalcium phosphate is more resorbable than β -tricalcium phosphate and hydroxyapatite. *Journal of Biomedical Material Research*, 59, 29-34.

Luthen, F., Bulnheim, U., Muller, P.D., Rychly, J., Jesswein, H. and, Barbara Nebe, J.G. (2007) Influence of manganese ions on cellular behavior of human osteoblasts in vitro. *Biomolecule Engineering*, 24, 531-536.

Matsunaga, K. and, Murata, H. (2009) Strontium Substitution in Bioactive Calcium Phosphates: A First-Principles Study. *Journal of Physical Chemistry B*, 113, 3584-3589.

Medvecky, L., Stulajterova, R., Parilak, L., Trpcevska, J., Durisin, J. and, Barinov, S.M. (2006) Influence of manganese on stability and particle growth of hydroxyapatite in simulated body fluid. *Colloid and Surface A: Physical Engineering Aspects*, 281, 221-229.

Miola, M., Brovarone, C.V., Maina, G., Rossi, F., Bergandi, L., Ghigo, D., Saracino, S., Maggiora, M., Canuto, R.A., Muzio, G. and, Verne, E. (2014) In vitro study of manganese-doped bioactive glasses for bone regeneration. *Material Science and Engineering C*, 38, 107-118.

Mladenovic, Z., Johansson, A., Willman, B., Shahabi, K., Björn, E., Ransjö, M.

(2014) Soluble silica inhibits osteoclast formation and bone resorption *in vitro*. *Acta Biomaterialia*, 10, 406–418.

Mourino, V., Cattalini, J.P. and, Boccaccini, A.R. (2012) Metallic ions as therapeutic agents in tissue engineering scaffolds: an overview of their biological applications and strategies for new developments. *Journal of Royal Society of Interface*, 9, 401-419.

Myrissa, A., Agha, N.A., Lu, Y., Martinelli, E., Eichler, J., Szakacs, G., Kleinhans, C., Willumeit-Romer, R., Schafer, U. and, Weinberg, A.-M. (2016) In vitro and in vivo comparison of binary Mg alloys and pure Mg. *Material Science and Engineering C*, 61, 865-874.

Obata, A., Tokuda, S. and, Kasuga, T. (2009) Enhanced in vitro cell activity on silicon-doped vaterite/poly(lactic acid) composites. *Acta Biomaterialia*, 5, 57-62.

Pabbruwe, M.B., Standard, O.C., Sorrell, C.C. and, Howlett, C.R. (2004) Bone formation within alumina tubes: effect of calcium, manganese, and chromium dopants. *Biomaterials*, 25, 4901-4910.

Parra, J., Garcia-Paez, I.H., DeAza, A.H., Baudin, C., Martin, M.R. and, Pena, P. (2017) In vitro study of the proliferation and growth of human fetal osteoblasts on Mg and Si co-substituted tricalcium phosphate ceramics. *Journal of Biomedical Material*

Research Part A, 105A, 2266-2275.

Saugo, M., Brugnoli, L.I., Flamini, D.O. and, Saidman, S.B. (2018)

Immobilization of antibacterial metallic cations (Ga^{3+} , Zn^{2+} and Co^{2+}) in a polypyrrole coating formed on Nitinol. *Material Science and Engineering C*, 86, 62-69.

Sugiura, Y. Munar, M.L. and, Ishikawa, K. (2018) Fabrication of octacalcium phosphate block through a dissolution-precipitation reaction using a calcium sulphate hemihydrate block as a precursor. *Journal of Materials Science: Materials in Medicine*, 29, 151-159.

Sugiura, Y. and, Makita, Y. (2018) Sodium Induces Octacalcium Phosphate Formation and Enhances Its Layer Structure by Affecting the Hydrous Layer Phosphate. *Crystal Growth & Design*, 18, 6165-6171.

Sugiura, Y. and, Makita, Y. (2019) Sodium inhibits the formation of ammonium-substituted solid solutions of octacalcium phosphate (OCP) formation by filling its substitution site. *Dalton Transactions*, 48, 1386-1391.

Sugiura, Y., Saito, Y., Endo, T. and, Makita, Y. (2019) Effect of the Ionic Radius of Alkali Metal Ions on Octacalcium Phosphate Formation via Different Substitution Modes. *Crystal Growth & Design*, 19, 4162-4171.

Sugiura, Y., Niitsu, K., Saito, Y., Endo, T. and, Horie, M. (2021) Inorganic process

for wet silica-doping of calcium phosphate. RSC Advances, 11, 12330.

Suzuki, O. (2010) Octacalcium phosphate: Osteoconductivity and crystal chemistry. Acta Biomaterialia 6 (2010) 3379-3387.

Valanezhad, A., Tsuru, K., Maruta, M., Kawachi, G., Matsuya, S. and, Ishikawa, K. (2010) Zinc phosphate coating on 316L-type stainless steel using hydrothermal treatment. Surface Coating Technology, 205, 2538-2541.

Vereecke, G. and, Lemaitre, J. (1990) Calculation of the solubility diagrams in the system $\text{Ca}(\text{OH})_2\text{-H}_3\text{PO}_4\text{-KOH-HNO}_3\text{-CO}_2\text{-H}_2\text{O}$. Journal of Crystal Growth, 104, 820-832.

Wang, L. and, Nancollas, G.H. (2008) Calcium Orthophosphate: Crystallization and Dissolution. Chemical Reviews, 108, 4628-4669.

Wei, D., Du, Q., Wang, S., Cheng, S., Wang, Y., Li, B., Jia, D. and, Zhou, Y. (2019) Rapid Fabrication, Microstructure, and in Vitro and in Vivo Investigations of a High-Performance Multilayer Coating with External, Flexible, and Silicon-Doped Hydroxyapatite Nanorods on Titanium. ACS Biomaterial Science and Engineering, 5, 4244-4262.

Zhong, J., Yi, F., Gao, A., Shu, D., Huang, Y., Li, Z., Zhu, W., He, C., Meng, T., Zhao, S. (2017) Preparation of 3D Reduced Graphene Oxide/MnO₂ Nanocomposites

through a Vacuum-Impregnation Method and Their Electrochemical Capacitive Behavior.

ChemElectroChem 4(5), DOI: 10.1002/celec.201600836.

Figure captions

Figure 1. pH values of the treated solutions at 1 (solid) and 3 (open) days as a function of the Na concentrations: ●, ○: 0 mmol/L Mn; ◆, ◇: 10 mmol/L Mn; ■, □: 20 mmol/L Mn. ▲; △: 50 mmol/L Mn; and ▼, ▽: 100 mmol/L Mn.

Figure 2. Wide-range XRD patterns of the treated samples at 1 day: (a) 0 mmol/L Mn; (b) 10 mmol/L Mn; (c) 20 mmol/L Mn; (d) 50 mmol/L Mn; and (e) 100 mmol/L Mn. ★: MnO(OH). ▼: HAp. ●: OCP-Mn,Na.

Figure 3. Small-angle XRD patterns of the treated samples at 1 day: (a) 0 mmol/L Mn; (b) 10 mmol/L Mn; (c) 20 mmol/L Mn; (d) 50 mmol/L Mn; and (e) 100 mmol/L Mn. ★: MnO(OH). ▼: HAp. ●: OCP-Mn,Na.

Figure 4. Wide-range XRD patterns of the treated samples at 3 days: (a) 0 mmol/L Mn; (b) 10 mmol/L Mn; (c) 20 mmol/L Mn; (d) 50 mmol/L Mn; and (e) 100 mmol/L Mn. ★: MnO(OH). ▼: HAp. ●: OCP-Mn,Na.

Figure 5. Small-angle XRD patterns of the treated samples at 3 days: (a) 0 mmol/L Mn;

(b) 10 mmol/L Mn; (c) 20 mmol/L Mn; (d) 50 mmol/L Mn; and (e) 100 mmol/L Mn. ★: MnO(OH). ▼: HAp. ●: OCP-Mn,Na.

Figure 6. Phase diagrams of the samples in the Na–Mn systems at 1 (a) and 3 (b) days:

●: OCP; ○: HAp with OCP; ◇: DCPD; ▽: OCP with manganite; ★: OCP-Mn,Na with calcite; ◆: DCPD and OCP; *: OCP-Mn,Na, DCPD, and calcite; ×: OCP, calcite and, manganite; and +: OCP-Mn,Na, manganite and, calcite.

Figure 7. Lattice constants of the OCP samples as a function of Mn-Na concentration as calculated by the Rietveld method using Brown et al. (1962) as the initial model. ●: Mn-0 mmol/L, ○: Mn-10 mmol/L, ◆: Mn-20 mmol/L, ▲: Mn-50 mmol/L, and ▼: Mn-100 mmol/L; (a) *a*-axis; 1day, (b) *b*-axis; 1day, (c) *c*-axis; 1day, (d) *a*-axis; 3days, (e) *b*-axis; 3days and (f) *c*-axis; 3days.

Figure 8. XRD patterns of the CaCO₃ optimization experiments: (a) wide-range and (b) small-angle.

Figure 9. XPS spectra of the samples. (a) whole spectrum (survey); (b) Ca 2*p*; (c) P 2*p*;

(d) Na 1s (the blue arrow indicates a peak in the spectrum of OCP–Na); and (e) Mn 2p.

Figure 10. FT-IR spectra of the samples: (a) wide-range; (b) main band (PO₄ adsorption region); and (c) P5 PO₄ vibration. The blue broken lines correspond to the PO₄ vibration. The red broken line depicts the P3 PO₄ vibration. The red solid circles correspond to the P5 PO₄ vibration. (Berry and Baddiel 1967)

Figure 11. TG (a) and DTA (b) curves of the samples. The blue and red broken arrows correspond to a significant weight loss that reflected significant DTA peaks.

Figure 12. SEM micrographs of (a, b) 0 mmol/L-Mn and 0 mol/L-Na, (c, d) 100 mmol/L-Mn and 0 mol/L, and (e, f) 100 mmol/L-Mn and 5 mol/L Na (OCP-Mn,Na).

Figure 13. XRD patterns of the samples treated with 5 mol/L of each metal chloride and 100 mmol/L Mn: (a) wide-range and (b) small-angle.

Figure 2.

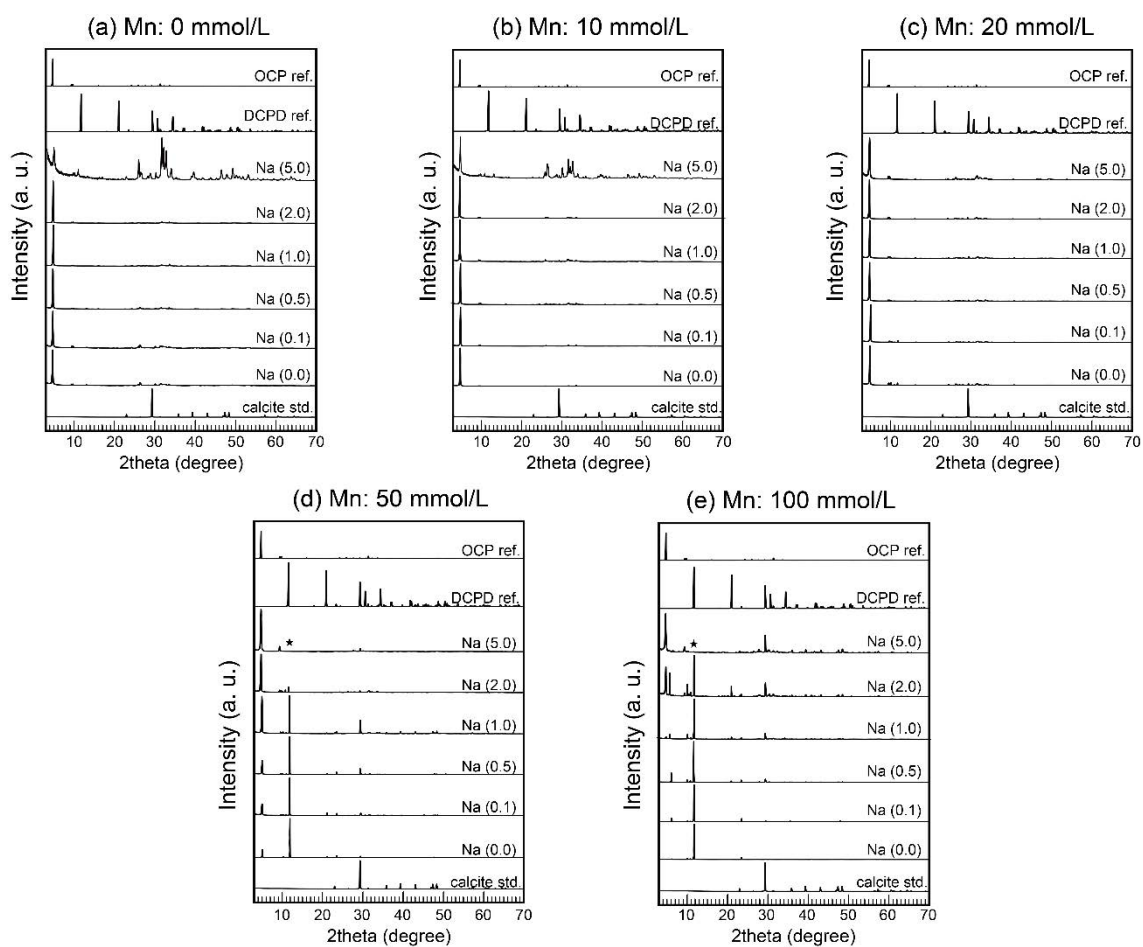


Figure 3.

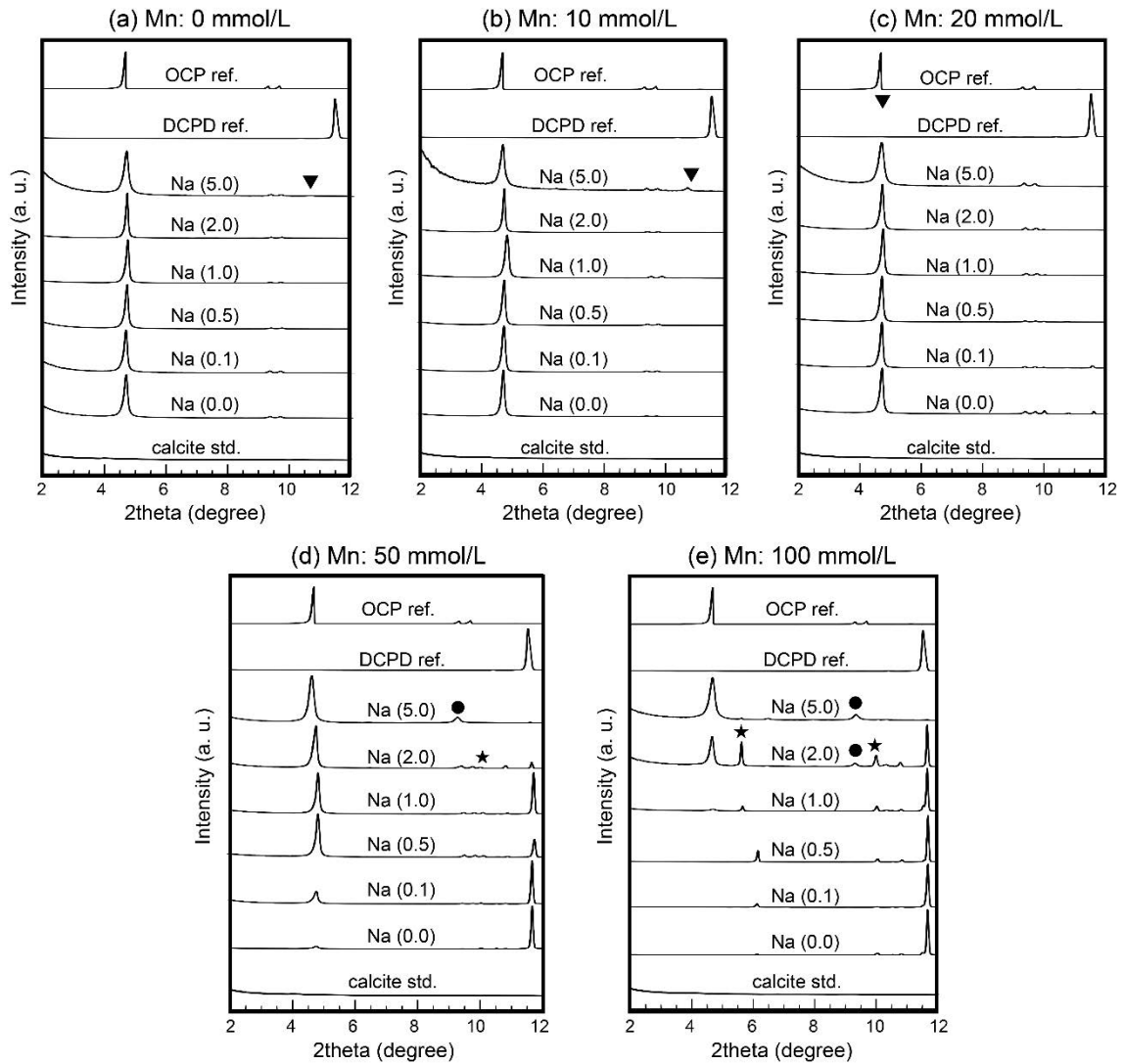


Figure 4.

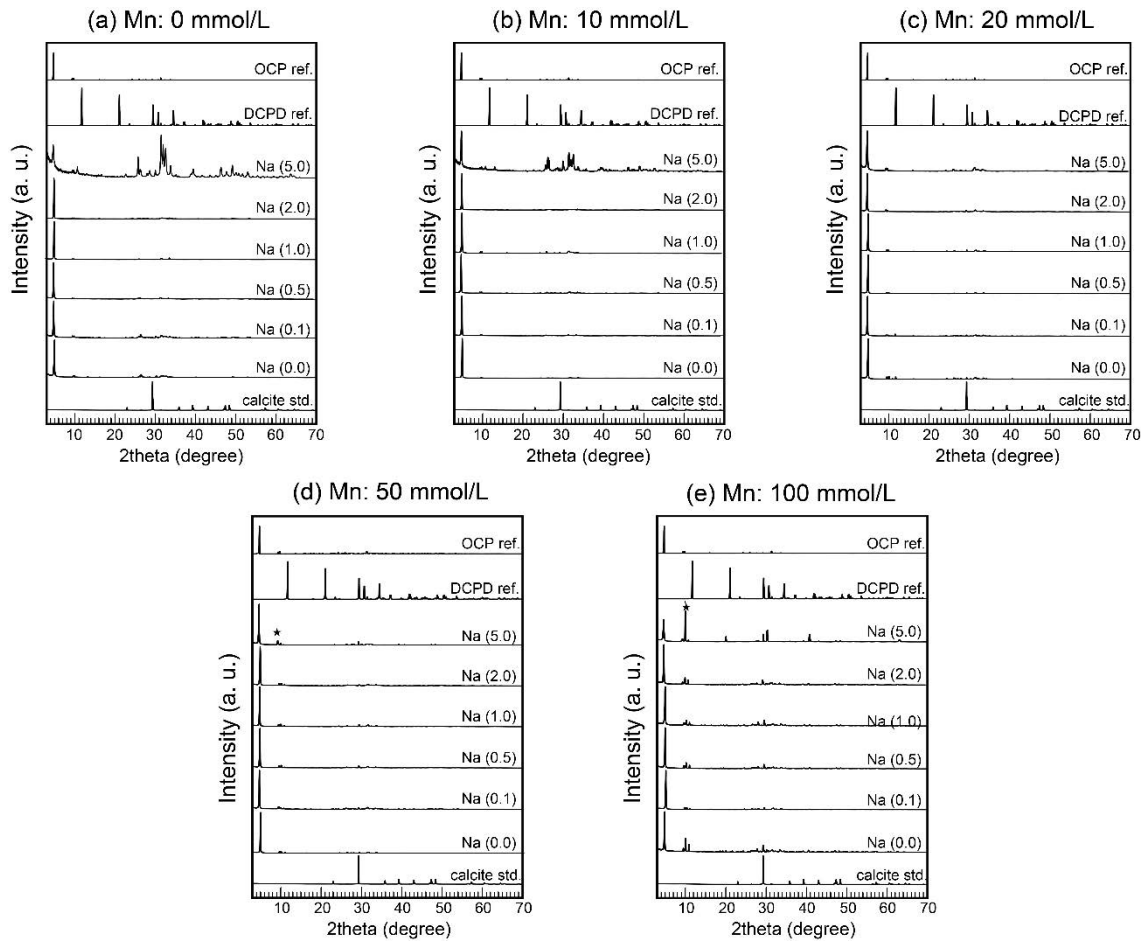


Figure 5.

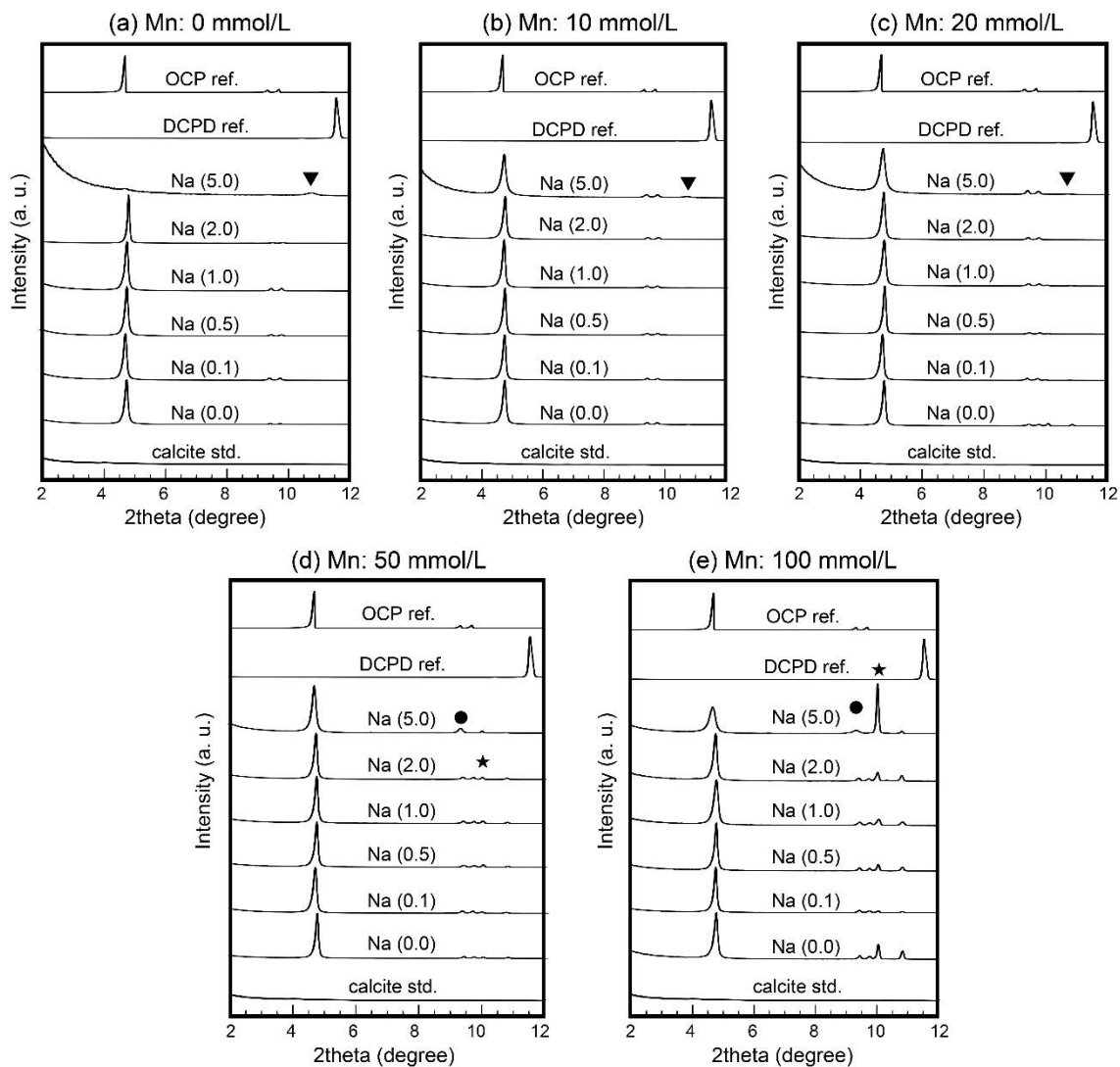


Figure 6.

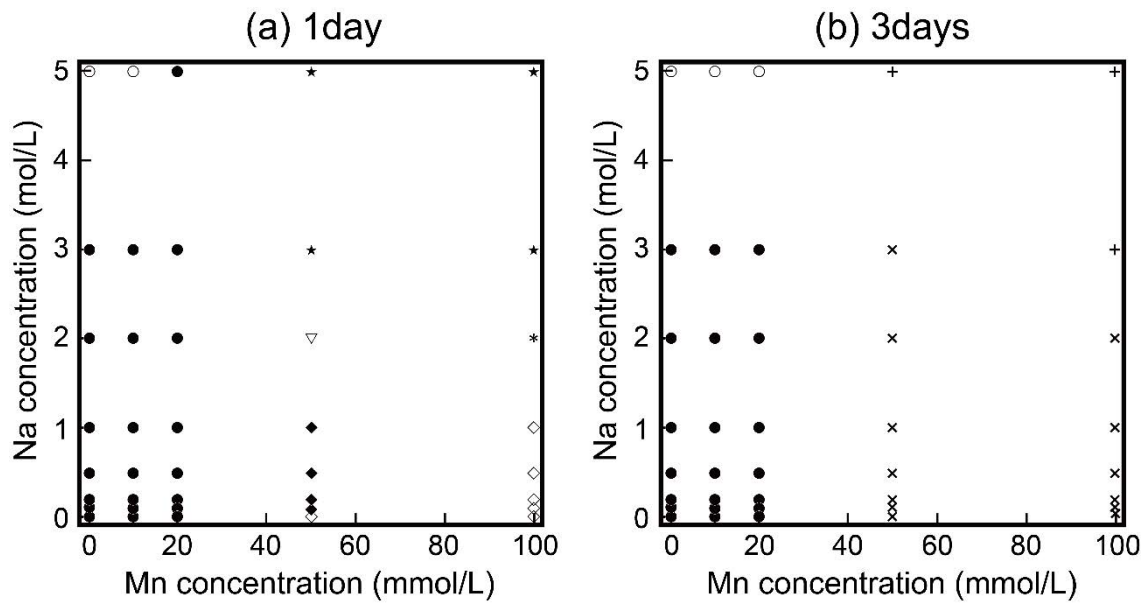


Figure 7.

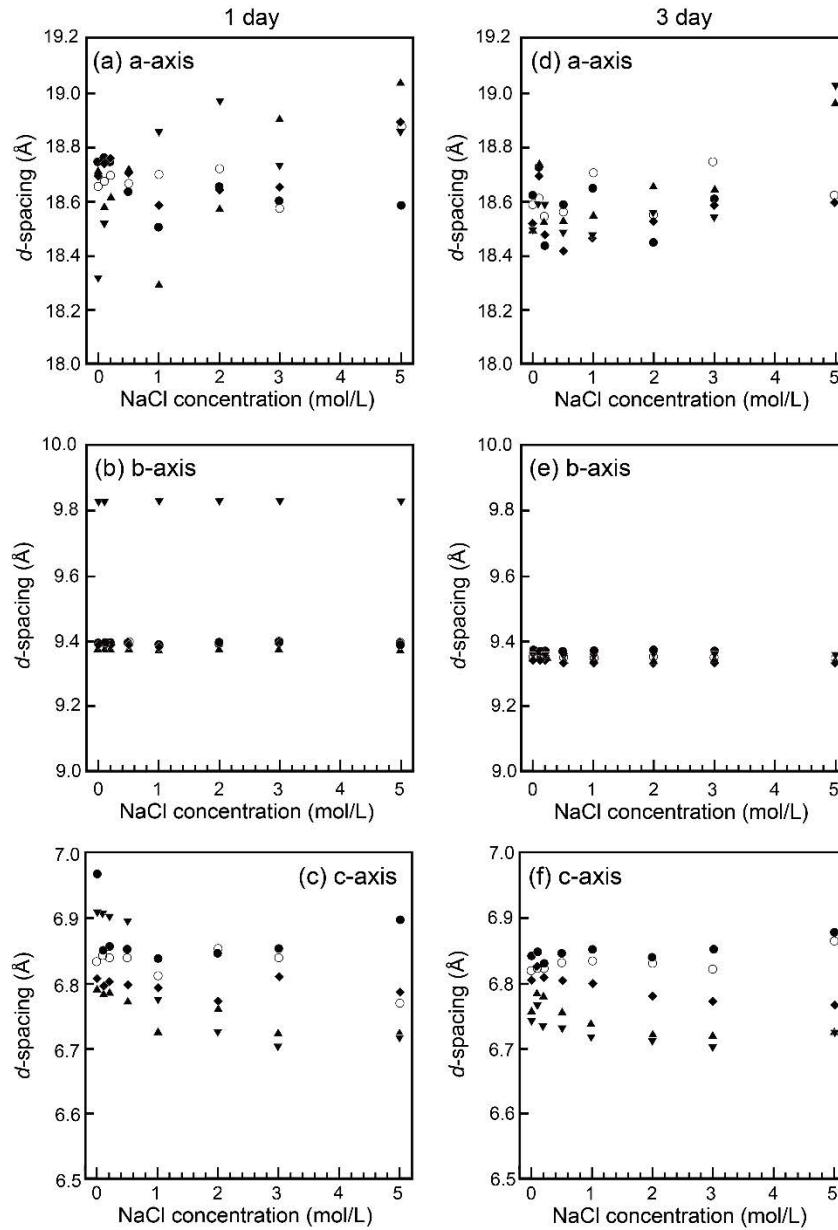


Figure 8.

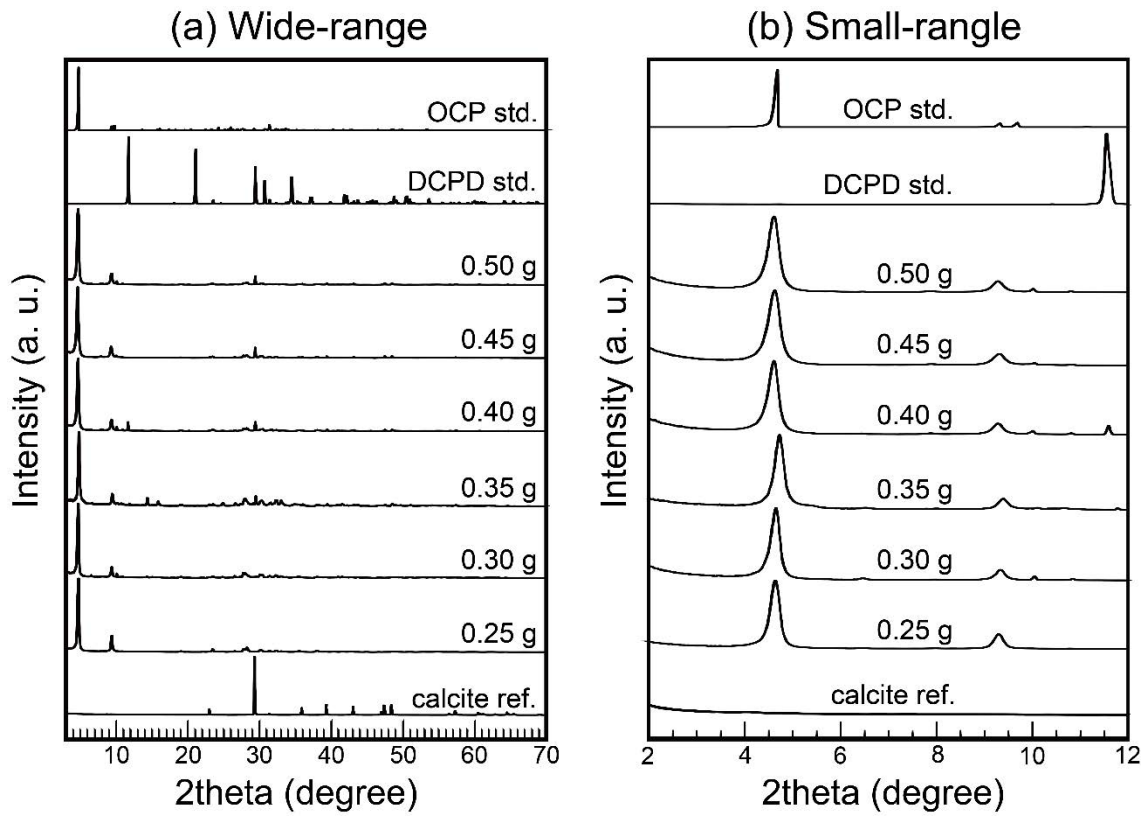


Figure 9.

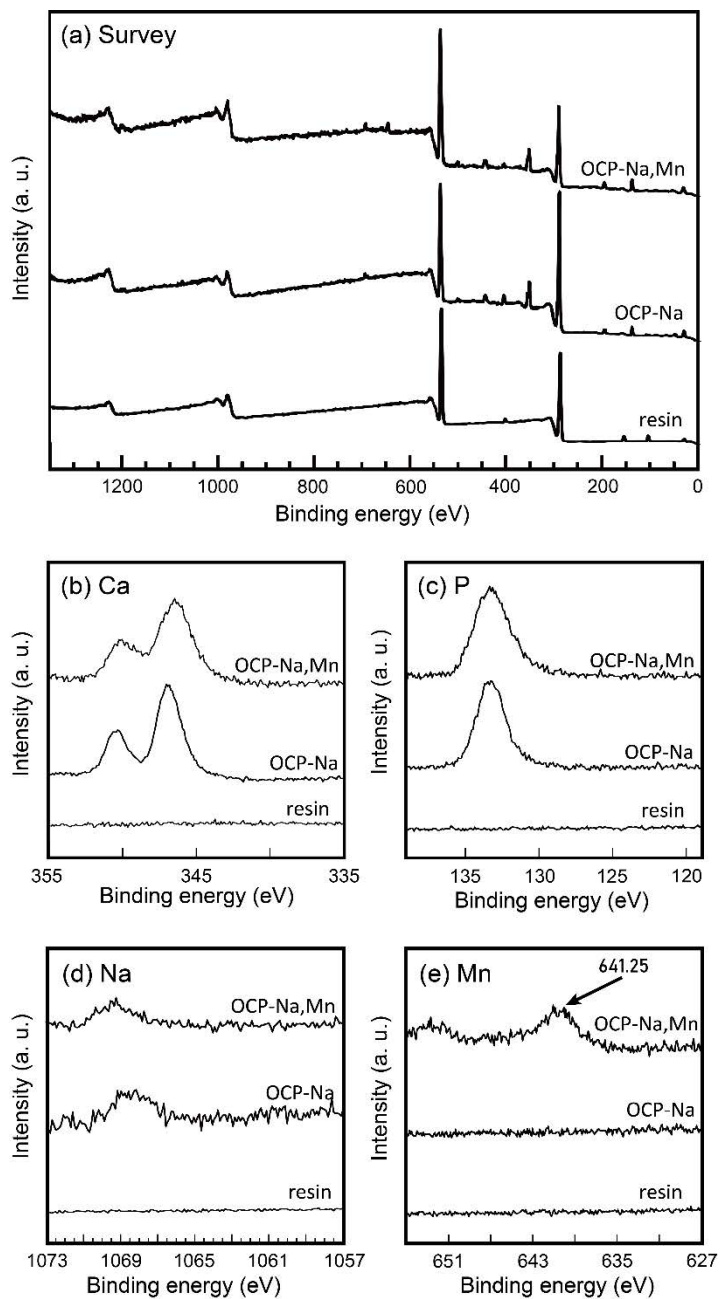


Figure 10.

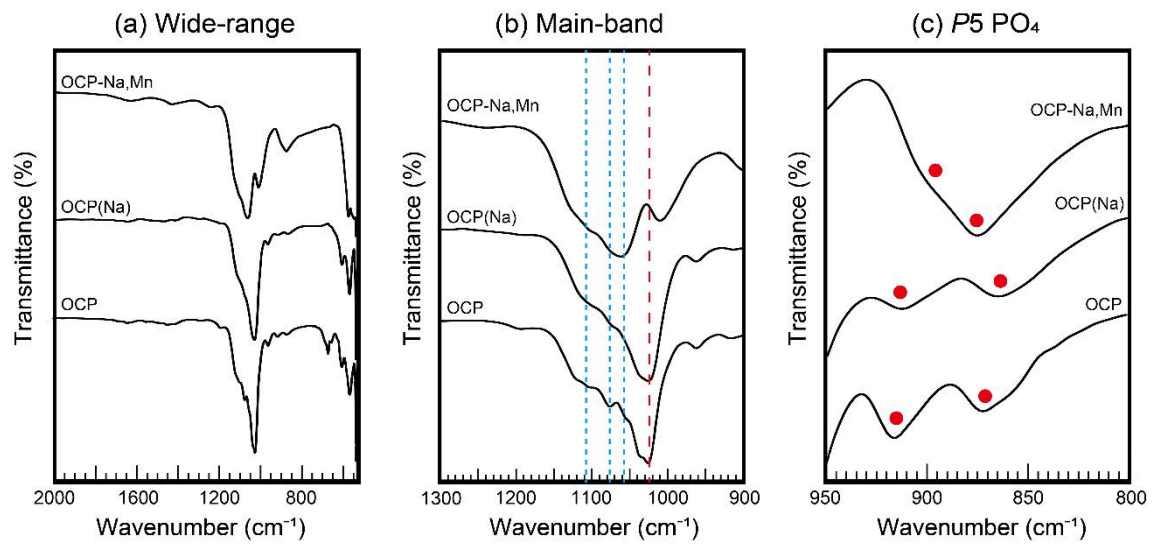


Figure 11.

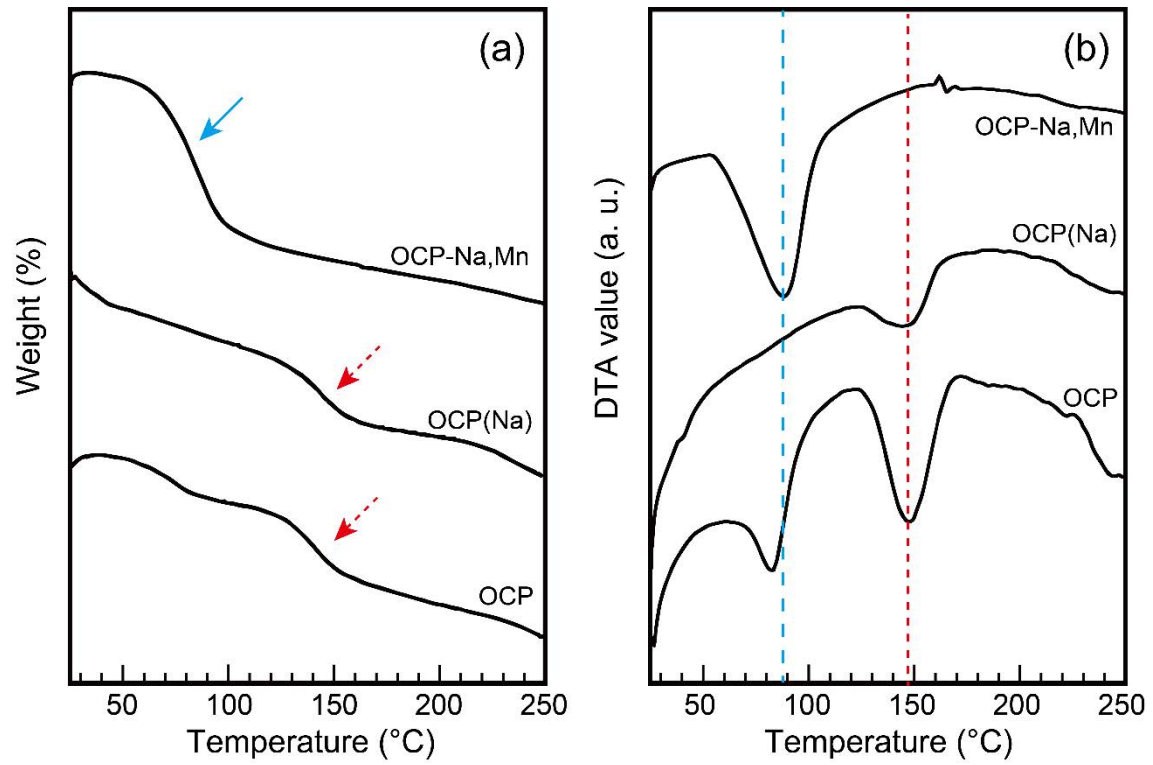


Figure 12.

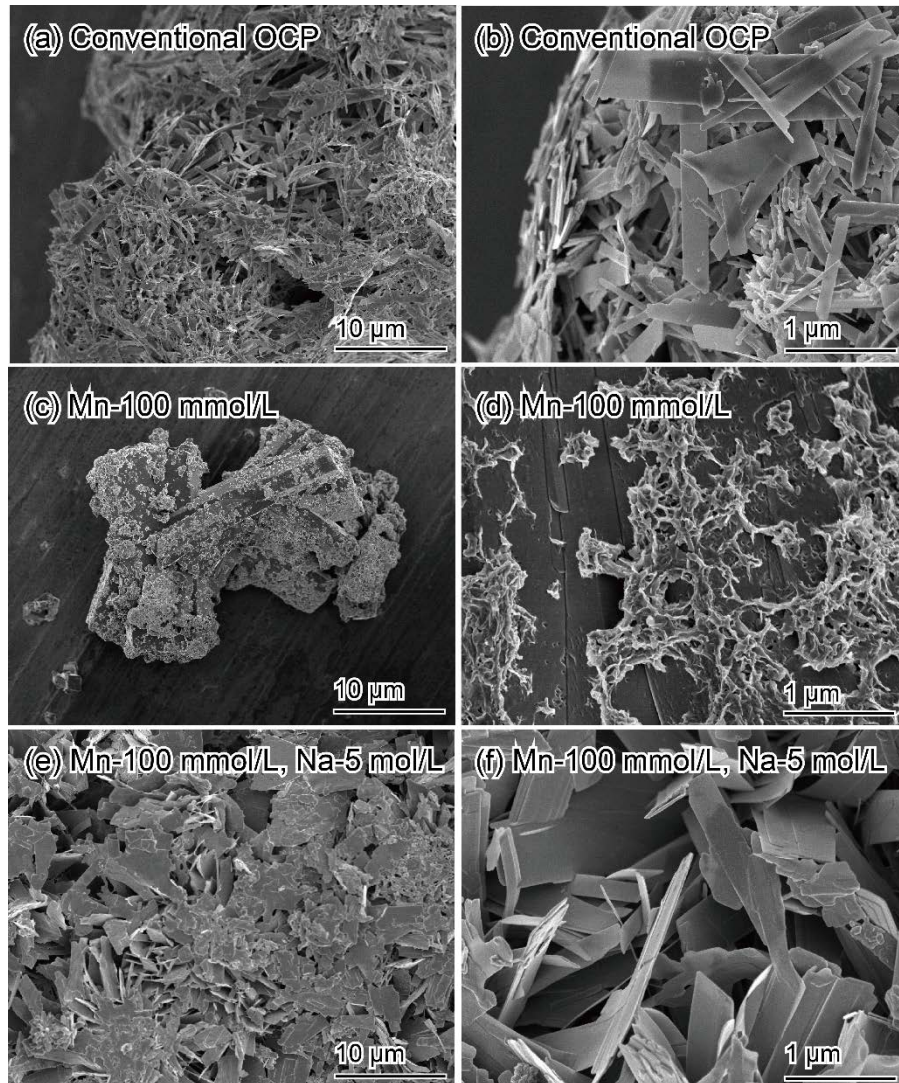


Figure 13.

